Journal of Power Sources 233 (2013) 6–13

Contents lists available at SciVerse ScienceDirect

Journal of Power Sources

journal homepage: www.elsevier.com/locate/jpowsour

# Sintering, phase composition and ionic conductivity of zirconia–scandia–ceria

R.L. Grosso, E.N.S. Muccillo*

*Energy and Nuclear Research Institute – IPEN, Av. Prof. Lineu Prestes, 2242, Cidade Universitária, S. Paulo 05508-000, SP, Brazil*

## HIGHLIGHTS

- $CeO_2$ addition to scandia-doped zirconia stabilizes the cubic structure up to 1000 °C.
- Overfiring results in degradation of the cubic phase and ionic conductivity.
- A fine microstructure is obtained with the two-stage method.

## ARTICLE INFO

*Article history:*
Received 20 August 2012
Received in revised form
19 November 2012
Accepted 23 January 2013
Available online 29 January 2013

*Keywords:*
Sintering
Densification
Crystalline structure
Solid electrolyte
Ionic conductivity

## ABSTRACT

The effects of the method of sintering on phase content, densification and ionic conductivity of zirconia stabilized with 10 mol% scandia and 1 mol% ceria are investigated varying dwell temperature and time. Thermodilatometry as well as sintered density results indicate a fast densification for temperatures above 1150 °C. The rhombohedric phase is detected in the 1150–1300 °C range depending on the sintering time. In conventionally sintered pellets, after 2 h at 1200 °C the material is cubic single-phase. For this method of sintering, high dwell temperatures and prolonged times lead to phase decomposition and consequent formation of the rhombohedric phase. For any specific relative density, the mean grain size of pellets sintered by the two-stage method is smaller than the conventionally sintered ones. The smaller mean grain size obtained for specimens sintered by the two-stage method precludes an improvement in the mechanical properties. The overall electrolyte conductivity determined by impedance spectroscopy for pellets sintered by both methods exhibits similar behavior over the whole temperature range (300–800 °C) of measurements.

© 2013 Elsevier B.V. All rights reserved.

## 1. Introduction

Scandia-stabilized zirconia is a solid electrolyte with potential application in intermediate-temperature solid oxide fuel cells, because of the combination of its physical and chemical properties specially the ionic conductivity and the chemical stability under severe environments [1–4]. The main drawback of this solid electrolyte is the complex nature of phase composition according to the phase diagram [5].

The highest value of ionic conductivity was obtained for 9 mol% $Sc_2O_3$ [3] along with high rate of thermal degradation, due to formation of the tetragonal structure in the cubic matrix [4,6,7]. For higher $Sc_2O_3$ contents a rhombohedric ($\beta$) phase with relatively low ionic conductivity was observed [3,4]. Several additives have been investigated as an approach to suppress the phase transition between the cubic and the rhombohedric structures, and relevant results came up with addition of cerium oxide [8]. Addition of small amounts of ceria (1 mol%) stabilized the cubic structure of the solid electrolyte. The ternary solid solution exhibits a slightly lower ionic conductivity compared to the single doped material.

A number of studies in the ternary system has been carried out so far. Wang et al. [9] identified by Raman spectroscopy the $t'$ phase in 10 mol% scandia stabilized zirconia with different additions of ceria prepared by chemical route. The thermal stability at 800 and 1000 °C up to 600 h of the composition containing 1 mol% ceria and 10 mol% scandia, hereafter denoted simply as 10Sc1CeSZ, was demonstrated by Lee et al. [10]. Recently Tu et al. [11] reported the properties of films of 10Sc1CeSZ prepared by the sol–gel method and concluded that the main characteristics of the starting powders played a major role on the densification of the films. Yarmolenko et al. [12] compared the densification and phase composition of 10Sc1CeSZ commercial powders prepared by different chemical routes. Significant differences were observed evidencing the influence of the microstructure on the final phase composition. The mechanical properties of 10Sc1CeSZ were studied by Orlovskaya et al. [13], and a straight relationship between the sintering parameters and the hardness was found.

* Corresponding author. Tel.: +55 11 31339203; fax: +55 11 31339276.
*E-mail address:* enavarro@usp.br (E.N.S. Muccillo).

0378-7753/$ – see front matter © 2013 Elsevier B.V. All rights reserved.
http://dx.doi.org/10.1016/j.jpowsour.2013.01.140

In this work the effects of the sintering method on phase composition and ionic conductivity of 10Sc1CeSZ were systematically investigated taking into account the main parameters of sintering, i.e., dwell temperature and holding time. Several samples were prepared by the conventional and the two-stage methods and the structural characteristics and the ionic conductivity were evaluated by X-ray diffraction and impedance spectroscopy, respectively. In the two-stage method of sintering the samples are heated up to a relatively high temperature and immediately cooled down to the dwell temperature. Thus, this method can allow for co-firing the anode and the electrolyte of a solid oxide fuel cell reducing the production cost. In addition, the comparatively low dwell temperature results in a small grain size compared to that obtained with conventional sintering. Then, this method can provide additional improvement of the mechanical properties of the cell.

## 2. Experimental

### 2.1. Powder material and processing

Zirconia-10 mol% scandia and 1 mol% ceria (>99.9%, Fuel Cell Materials, FCM) with 11.5 $m^2\ g^{-1}$of specific surface area was used as-received.

Cylindrical compacts with 10 mm diameter and ~3 mm thickness were prepared by uniaxial pressing (45 MPa) followed by cold isostatic pressing (100 MPa). All sintering experiments were carried out in air in a box-type furnace (Lindberg 51524) with heating rate of 10 °C $min^{-1}$.

In conventional sintering experiments, the compacts were heated up to the desired dwell temperature, and after a specific holding time, they were cooled down to room temperature by turning off the furnace. In the two-stage sintering experiments the compacts were first heated up to a high temperature ($T_1$) for null holding time and cooled down at 30 °C $min^{-1}$ to the dwell temperature ($T_2$). After a specific holding time ($t_2$) at that temperature, the compacts were cooled down to room temperature by turning the furnace off.

### 2.2. Characterization methods

X-ray diffraction measurements were performed in a diffractometer (Bruker-AXS, D8 Advance) with Bragg-Brentano configuration using Cu $K_\alpha$ radiation and Ni filter. Powder materials as well as sintered pellets were measured in the 20–80° angular range with 0.05° step size and 2 s counting time. Phase identification was accomplished by comparison with JCPDS files # 89-5483 and 51-1604 corresponding to cubic and rhombohedric phases, respectively.

Linear shrinkage was measured by thermodilatometry (Setaram, Labsys) in cylindrical compacts prepared by uniaxial and isopressing (210 MPa). In these experiments the compacts were heated at 10 °C $min^{-1}$ up to 1380 °C and cooled down (20 °C $min^{-1}$) to room temperature in stagnant atmosphere of synthetic air.

Microstructural characterization was performed by scanning electron microscopy (Philips, XL30) observations using secondary electrons in the powder material and in polished and thermally etched surfaces of sintered pellets. The mean grain size, $G$, was estimated by the linear intercept method. Sintered density values were determined by both the geometric and the immersion ($\rho_h$) methods.

Ionic conductivity measurements were carried out by impedance spectroscopy (HP 4192A) in the 5 Hz to 13 MHz frequency range with 100 mV of applied AC signal. Silver and platinum were used as electrode materials in the low (from 300 to 450 °C) and high (from 450 to 850 °C) temperature ranges, respectively. Deconvolution of impedance spectroscopy spectra was performed with specially designed software [14] for data collected in the low temperature range. For high temperature data, only the overall ionic conductivity comprising grain and grain boundary contributions are reported.

## 3. Results and discussion

### 3.1. Powder and compact characterization

Fig. 1 shows scanning electron microscopy micrographs of the as-received powder material. The morphology of the powder consists of spherical agglomerates of varying sizes not exceeding 100 μm (Fig. 1a). These agglomerates are formed by submicron sized particles, as can be seen in the high magnification micrograph (Fig. 1b).

Fig. 2 shows the room temperature X-ray diffraction pattern of the powder material after heating up to 1000 °C. A single cubic phase (space group Fm3m) is identified with lattice parameter of 5.090 Å analogously to previous reported values [15,16]. This X-ray diffraction pattern is similar to that, not shown here, recorded in the as-received powder, thus ensuring the stability of the cubic phase during thermal cycling up to 1000 °C.

The linear shrinkage curve and its derivative of a compact with 45% of relative green density are shown in Fig. 3.

The linear shrinkage of the compact starts above 1050 °C. The total shrinkage up to 1380 °C amounts 21%, and the rate of shrinkage is maximum at 1180 °C. These results are in general agreement with those of the same composition prepared by coprecipitation [16] and flame spray [15].

### 3.2. Conventional sintering

Several sintering conditions were investigated for a detailed study of the densification with the dwell temperature and holding time. Fig. 4 shows the evolution of the relative density determined

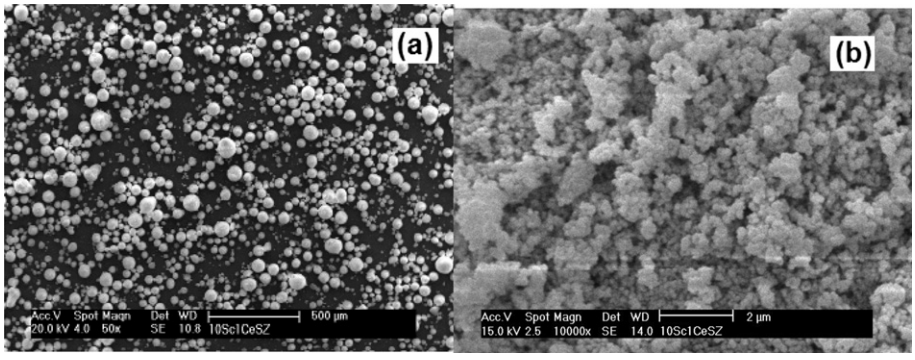


**Fig. 1.** SEM micrographs of the 10Sc1CeSZ powder with (a) low and (b) high magnification.

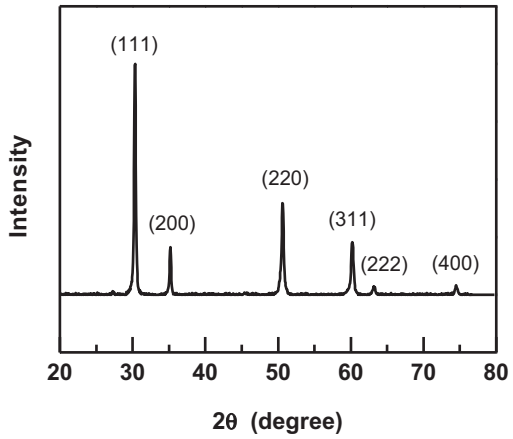


**Fig. 2.** Room temperature X-ray diffraction pattern of the 10Sc1CeSZ powder after thermal cycling up to 1000 °C.

by the geometric method as a function of the dwell temperature and holding time.

High values of density were obtained for dwell temperatures above 1150 °C. Below that temperature even holding times longer than 10 h resulted in only about 90% of relative density. In the 1150–1200 °C range a sharp increase of density was observed for a small (0.2 h) holding time. Then, fast densification occurs for temperatures higher than 1150 °C. The relative density of the compact sintered at 1350 °C for null holding time, for example, is 90%. At low temperatures (<1150 °C) the density increases continuously up to 15 h, but the kinetics of densification is slowed down after 2 h of holding time. For higher dwell temperatures (>1150 °C) the sintered density attains high values even for short times (~0.2 h) reaching a steady state at about 2 h.

Phase characterization of 10Sc1CeSZ compacts was initially conducted in samples sintered in the 1000–1400 °C range for null holding time. Fig. 5 shows the X-ray diffraction patterns obtained at room temperature. It may be clearly seen the characteristic diffraction peaks of the rhombohedric ($\beta$) phase, mainly those with Miller indexes (104) and (110) in the 48–53° 2$\theta$ range, for samples sintered from 1150 to 1300 °C. The compacts sintered below 1150 °C and above 1300 °C seem to exhibit only the reflections of the cubic structure. Similar results were reported in Ref. [12]. The intensity of diffraction peaks related to the rhombohedric phase is maximum at about 1200 °C and decreases for increasing temperatures.

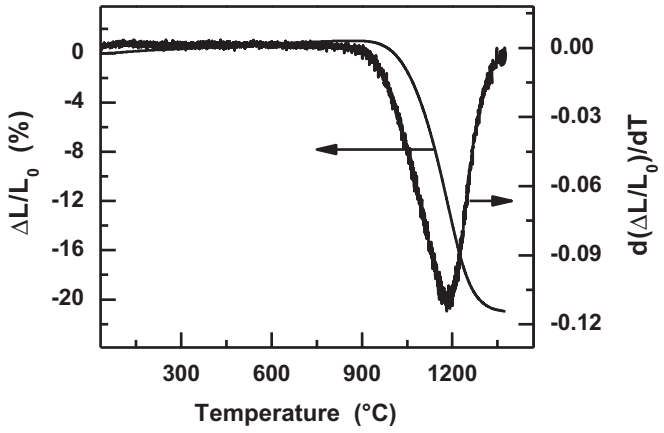


**Fig. 3.** Linear shrinkage and derivative curves of the 10Sc1CeSZ compact.

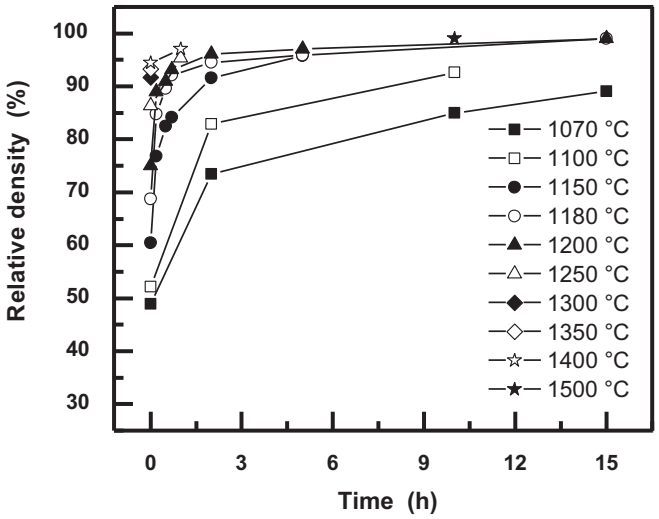


**Fig. 4.** Evolution of the relative density of 10Sc1CeSZ with sintering temperature and time.

The effect of the holding time at 1200 °C on the crystalline phase composition of 10Sc1CeSZ is shown in Fig. 6a. The fraction of the cubic phase increases with increasing holding time, so that after 2 h only the characteristics diffraction peaks of the cubic structure are detected. Fig. 6b highlights the angular region between 73 and 76° where the cubic and the tetragonal structures may be identified unambiguously. The high angle X-ray diffraction patterns evidence that no tetragonal structure is formed under these conditions.

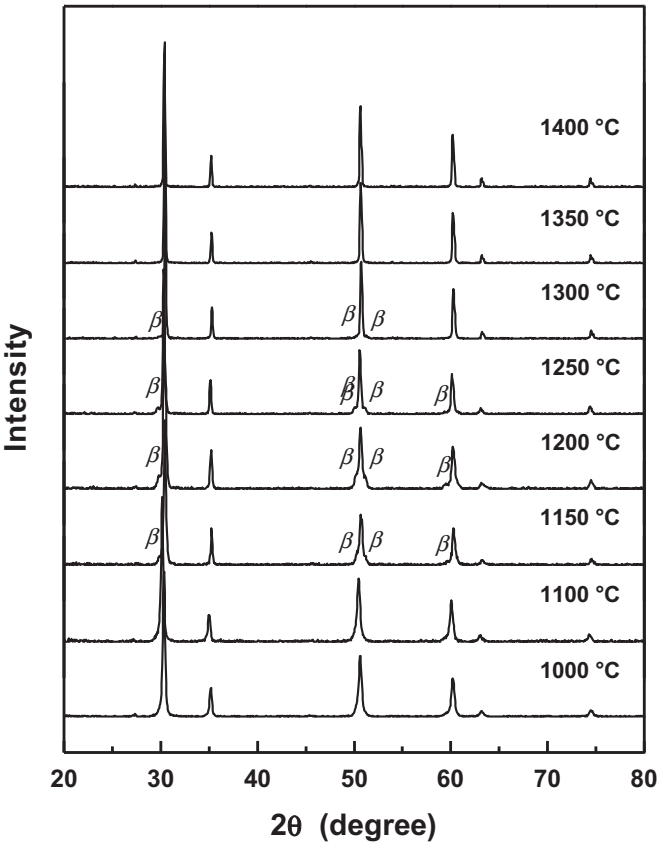


**Fig. 5.** X-ray diffraction patterns of 10Sc1CeSZ pellets sintered at several temperatures for null holding time.

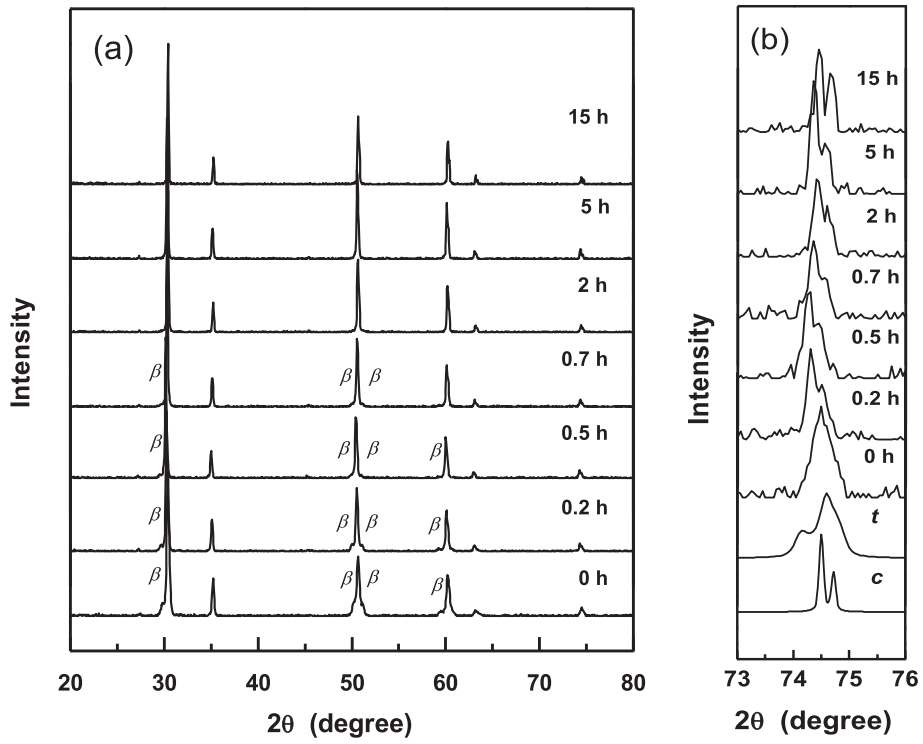


**Fig. 6.** X-ray diffraction patterns of 10Sc1CeSZ pellets sintered at 1200 °C for several holding times: (a) full angular range, (b) high-angle profiles; t = tetragonal, c = cubic.

Finally, the 10Sc1CeSZ samples were sintered for longer holding times at varying temperatures and the corresponding X-ray diffraction patterns are shown in Fig. 7. As can be seen, for sintering times of 10 and 15 h the rhombohedric phase was formed in samples sintered at low (<1200 °C) and high (1500 °C) temperatures.

The above results evidence that cerium oxide is an effective stabilizer of the cubic structure at room temperature, and in a subsequent thermal cycling up to ~1150 °C. Heat treatments in the ~1150 to ~1300 °C range result in partial transformation of the cubic to the rhombohedric structure. The fraction of β-phase formed depends on the time at that temperature owing to the diffusional nature of the reversible phase transition. Moreover, when the heat treatment is carried out at high temperatures and longer holding times, the well-known phenomenon of overfiring occurs with consequent degradation of the cubic structure.

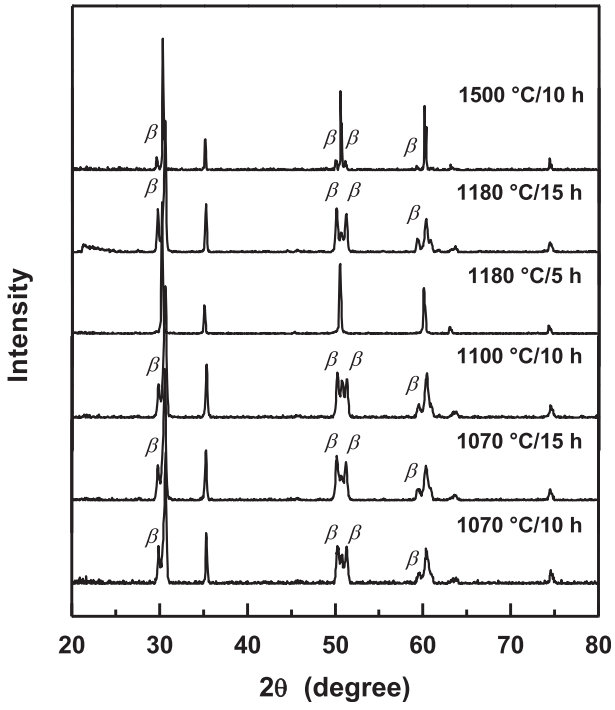


**Fig. 7.** X-ray diffraction patterns of 10Sc1CeSZ pellets sintered at selected temperatures for longer holding times.

Fig. 8 shows scanning electron microscopy micrographs of samples sintered at 1200 °C for (a) 0.5 and (b) 2 h, (c) 1250 °C for 1 h and (d) 1300 °C for null holding time. The morphology is quite homogeneous in these samples, with small fraction of porosity. The main difference among them is the mean grain size.

Table 1 summarizes the results on sintered density determined by the immersion method, mean grain size and crystalline structure of 10Sc1CeSZ. The symbols s and w associated to the β-phase stand, respectively, for strong and weak depending on the relative intensities of the diffraction peaks.

The mean grain size is in the submicrometer range for most of the investigated sintering conditions except for those at higher temperatures and/or longer times. The mean grain size of pellets sintered at 1070 °C for 10 and 15 h do not differ significantly. In contrast, sintering at 1200 °C promoted a gradual increase in the mean grain size with increasing holding time.

The whole set of results on densification, phase characterization and microstructure of 10Sc1CeSZ sintered by the conventional method evidences that a careful selection of the dwell temperature and time is a key role to obtain a cubic and single phase polycrystalline ceramic. Moreover, degradation of the cubic structure was revealed with longer holding times and high temperatures.

### 3.3. Two-stage sintering

In the two-stage sintering method the preliminary choice of $T_1$ is based on a relative density of at least 75% [17]. According to the

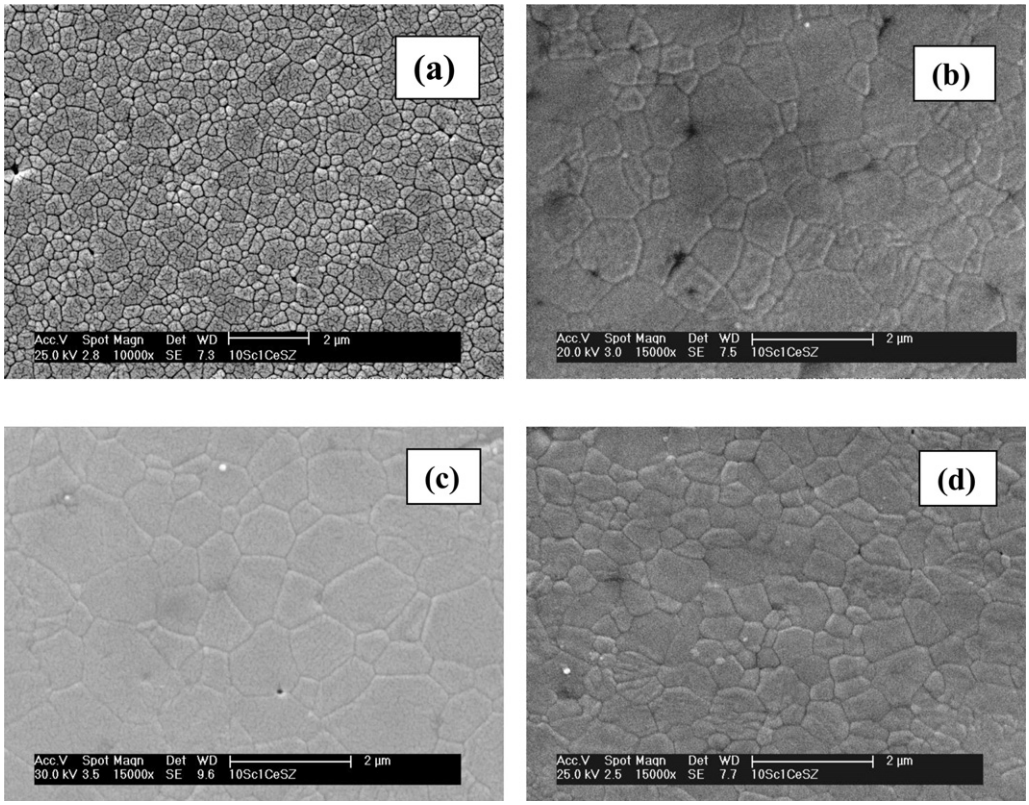


**Fig. 8.** SEM micrographs of polished and etched surfaces of 10Sc1CeSZ pellets sintered at: (a) 1200 °C/0.5 h, (b) 1200 °C/2 h, (c) 1250 °C/1 h and (d) 1300 °C for null holding time.

linear shrinkage curve (Fig. 3) the temperature of 1200 °C fulfills this requirement. For null holding time at that temperature, inspection of Fig. 5 shows, however, that a significant fraction of rhombohedric phase is found. Then, several temperatures ($T_1$ and $T_2$) and holding times ($t_2$) were exploited aiming to find alternative suitable sintering conditions. Fig. 9 shows X-ray diffraction patterns of 10Sc1CeSZ samples sintered by the two-stage method.

For $T_1$ and $T_2$ of 1200 °C and 1100 °C, respectively, increasing of the holding time resulted in an increased fraction of the rhombohedric phase, whereas for $T_1$ higher than 1300 °C only the cubic phase is detected independent on $T_2$ and $t_2$.

Fig. 10 shows scanning electron microscopy micrographs of samples sintered by the two-stage method. The main features are polygonal grains with submicrometer grain size. Porosity decreases significantly with increase in $T_2$ from 1070 to 1100 °C.

Values of sintered density, mean grain size and phase composition are listed in Table 2. According to these data, the effect of the holding time on the mean grain size depends on $T_1$ and $T_2$. At 1070 °C ($T_2$), for example, the increase of $t_2$ (5, 10 and 15 h) reveals no significant variation of the mean grain size. For $T_2$ equal to 1100 °C, $G$ increases with increasing holding times. Finally, when $T_1$ is equal to or higher than 1350 °C, the mean grain size increases with both $T_2$ and $t_2$.

These results are in general agreement with the proposed methodology [17], where inside a specific range of temperature and time, called "kinetic window", no grain growth is observed in the final stage of sintering. Outside this range, no densification (low temperature) or grain growth (high temperature) are expected to occur.

The evolution of the mean grain size with the relative density is depicted in Fig. 11 for pellets sintered by the two-stage method (empty symbols). The numbers represent the holding time. For comparison purposes, $G$ values for samples sintered by the conventional method are also plotted in this figure (full symbols). In this case, numbers over experimental points indicate the sintering temperature (null holding time).

Results in Fig. 11 show that for a fixed relative density value, the mean grain size of 10Sc1CeSZ samples sintered by the two-stage method is lower than that for conventionally sintered ceramics even outside the kinetic window. Thus, although the two-stage sintering method was not effective to produce a cubic and simultaneously nanosized 10Sc1CeSZ ceramic, it proved to be useful for

**Table 1**
Relative sintered density, mean grain size and crystalline structure of 10Sc1CeSZ pellets sintered at several dwell temperatures and holding times by the conventional method.

| $T$ (°C) | Time (h) | $\rho_h$ (%) | Mean grain size (μm) | Structure[c] |
|---|---|---|---|---|
| 1070 | 10 | 89.9 ± 0.3 | 0.30 ± 0.03 | $c + \beta$ (s) |
| | 15 | 92.7 ± 0.3 | 0.32 ± 0.05 | $c + \beta$ (s) |
| 1200 | 0 | 75.0 ± 0.3[a] | ~0.1[b] | $c + \beta$ (w) |
| | 0.2 | 90.4 ± 0.3 | 0.32 ± 0.05 | $c + \beta$ (w) |
| | 0.5 | 96.6 ± 0.3 | 0.53 ± 0.06 | $c + \beta$ (w) |
| | 0.7 | 96.7 ± 0.3 | 0.54 ± 0.09 | $c + \beta$ (w) |
| | 2 | 99.9 ± 0.5 | 0.67 ± 0.12 | $c$ |
| | 5 | 99.9 ± 0.3 | 0.70 ± 0.13 | $c$ |
| | 15 | 99.7 ± 0.5 | 1.42 ± 0.22 | $c$ |
| 1250 | 0 | 85.4 ± 0.4 | 0.36 ± 0.05 | $c + \beta$ (w) |
| | 1 | 98.4 ± 0.3 | 0.73 ± 0.14 | $c$ |
| 1300 | 0 | 93.2 ± 0.8 | 0.52 ± 0.08 | $c + \beta$ (w) |
| 1350 | 0 | 97.8 ± 0.3 | 0.91 ± 0.17 | $c$ |
| 1400 | 0 | 99.5 ± 0.2 | 1.51 ± 0.29 | $c$ |
| | 1 | 99.3 ± 0.5 | 2.28 ± 0.40 | $c$ |
| 1500 | 10 | 99.9 ± 0.4 | 4.94 ± 0.86 | $c + \beta$ (w) |

[a] Relative geometric density.
[b] Value estimated from the fractured surface.
[c] $c$ = cubic; $\beta$ = rhombohedral; s = strong, w = weak.

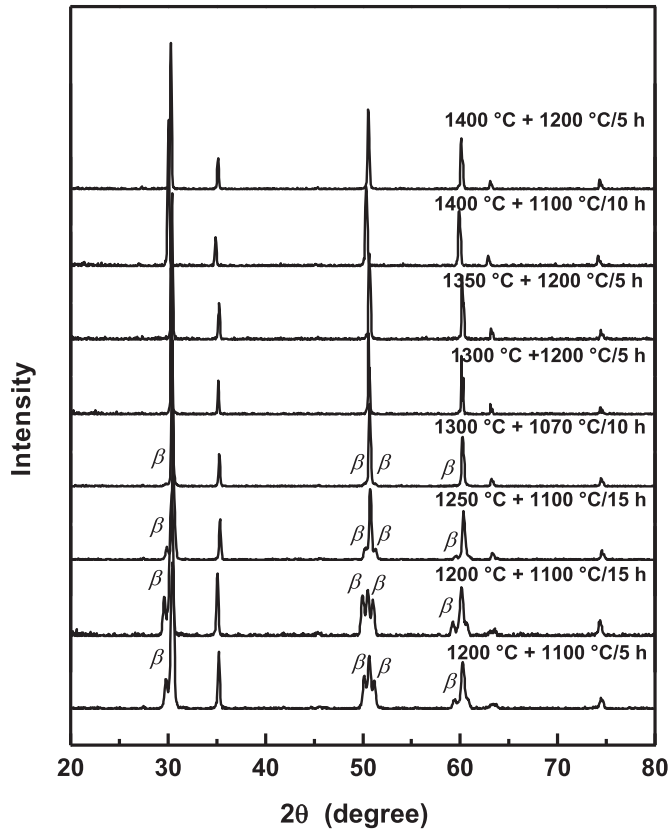


**Fig. 9.** X-ray diffraction patterns of 10Sc1CeSZ pellets sintered by the two-stage method.

obtaining a fine microstructure, which should favor the mechanical properties.

### 3.4. Ionic conductivity

The ionic conductivity was determined by impedance spectroscopy on pellets with high relative density (>95%). In the low-temperature range (<450 °C) the impedance diagrams could be deconvoluted and a careful analysis of the grain and grain boundary contributions to the overall electrolyte conductivity was carried out. Fig. 12a shows $[-Z''(\omega)\times Z'(\omega)]$ diagrams of samples sintered by the conventional method recorded at 380 °C. For all impedance diagrams, numbers over experimental points stand for the logarithm of the frequency (Hz), and the diagrams were normalized for sample dimensions.

**Table 2**
Relative sintered density, mean grain size and crystalline structure of 10Sc1CeSZ pellets sintered at several dwell temperatures and holding times by the two-stage method.

| $T_1$ (°C) | $T_2$ (°C) | $t_2$ (h) | $\rho_h$ (%) | Mean grain size (μm) | Structure[b] |
|---|---|---|---|---|---|
| 1200 | 1000 | 5 | 76.7 ± 0.25[a] | – | $c+\beta$ (s) |
| | 1050 | 5 | 82.1 ± 0.42[a] | – | $c+\beta$ (s) |
| | 1070 | 5 | 88.3 ± 0.47 | 0.24 ± 0.03 | $c+\beta$ (s) |
| | 1100 | 5 | 89.7 ± 0.49 | 0.29 ± 0.04 | $c+\beta$ (s) |
| 1200 | 1070 | 10 | 99.0 ± 0.23 | 0.25 ± 0.05 | $c+\beta$ (s) |
| | 1100 | 10 | 98.0 ± 0.21 | 0.35 ± 0.05 | $c+\beta$ (s) |
| 1200 | 1070 | 15 | 98.4 ± 0.31 | 0.28 ± 0.05 | $c+\beta$ (s) |
| | 1100 | 15 | 99.9 ± 0.39 | 0.44 ± 0.12 | $c+\beta$ (s) |
| 1250 | 1070 | 15 | 98.3 ± 0.44 | – | $c+\beta$ (s) |
| | 1100 | 15 | 94.0 ± 0.30 | – | $c+\beta$ (s) |
| 1300 | 1100 | 5 | 99.4 ± 0.19 | – | $c+\beta$ (w) |
| | 1200 | 5 | 99.9 ± 0.53 | 0.79 ± 0.17 | $c$ |
| 1300 | 1070 | 10 | 98.6 ± 0.18 | – | $c+\beta$ (w) |
| | 1100 | 10 | 95.0 ± 0.35 | – | $c+\beta$ (w) |
| 1300 | 1100 | 15 | 97.8 ± 0.20 | – | $c+\beta$ (w) |
| 1350 | 1200 | 2 | 99.9 ± 0.24 | 0.74 ± 0.14 | $c$ |
| 1350 | 1200 | 5 | 99.9 ± 0.82 | 0.99 ± 0.17 | $c$ |
| 1400 | 1200 | 2 | 99.9 ± 0.22 | 1.27 ± 0.23 | $c$ |
| 1400 | 1100 | 5 | 99.3 ± 0.27 | 1.12 ± 0.14 | $c$ |
| | 1200 | 5 | 99.9 ± 0.27 | 1.08 ± 0.19 | $c$ |
| 1400 | 1100 | 10 | 98.6 ± 0.23 | – | $c$ |

[a] Relative geometric density.
[b] $c$ = cubic; $\beta$ = rhombohedral; s = strong, w = weak.

The impedance diagrams consist of two well-resolved semicircles attributed to the grain resistivity (high frequency) and blocking effect at the grain boundaries (low frequency). The main difference in the impedance diagrams of Fig. 12a is the higher resistivity of the pellet sintered for the shortest time, i.e. containing the rhombohedric phase, which is known to exhibit higher resistivity than the cubic structure [14].

Fig. 12b shows impedance spectroscopy diagrams of samples sintered by the two-stage method recorded at 381 °C. In this case, the pellet sintered at 1300 °C followed by 1200 °C for 5 h exhibits a slightly higher resistivity than the others. This result suggests that this sample has a small fraction of the β-phase, which could not be fully revealed by X-ray diffraction experiments due to the limitations of this technique.

Arrhenius plots of the grain conductivity of some sintered pellets are shown in Fig. 13a.

The fitted straight lines in the Arrhenius plots of the grain conductivity of both conventionally and two-stage sintered samples are parallel to each other indicating equal activation energy

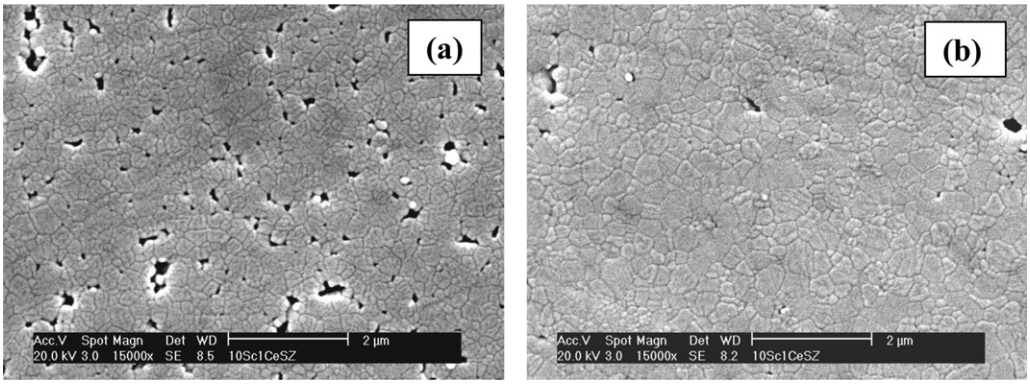


**Fig. 10.** SEM micrographs of polished and etched surfaces of 10Sc1CeSZ pellets sintered at: (a) 1200 °C + 1070 °C/5 h and (b) 1200 °C + 1100 °C/5 h.

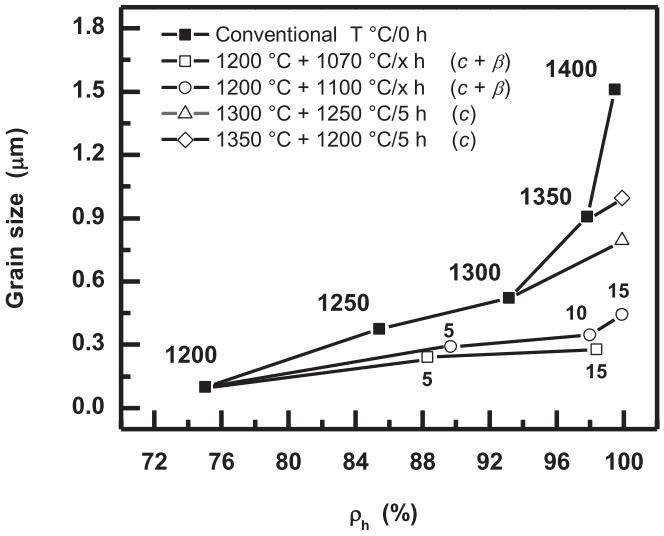


**Fig. 11.** Evolution of the mean grain size with the relative density of 10Sc1CeSZ pellets sintered by the conventional (full symbol) and two-stage (empty symbols) methods. Numbers over full symbols are the temperature (null holding time), and those over empty symbols represent the holding time ($t_2$).

values. The magnitude of the grain conductivity is fairly similar for all pellets except the one sintered at 1200 °C for 0.5 h, to which the conductivity is slightly lower.

Arrhenius plots of the grain boundary conductivity of these pellets are shown in Fig. 13b.

Increase of the temperature (two-stage sintered samples) or of the dwell time (conventionally sintered samples) promotes

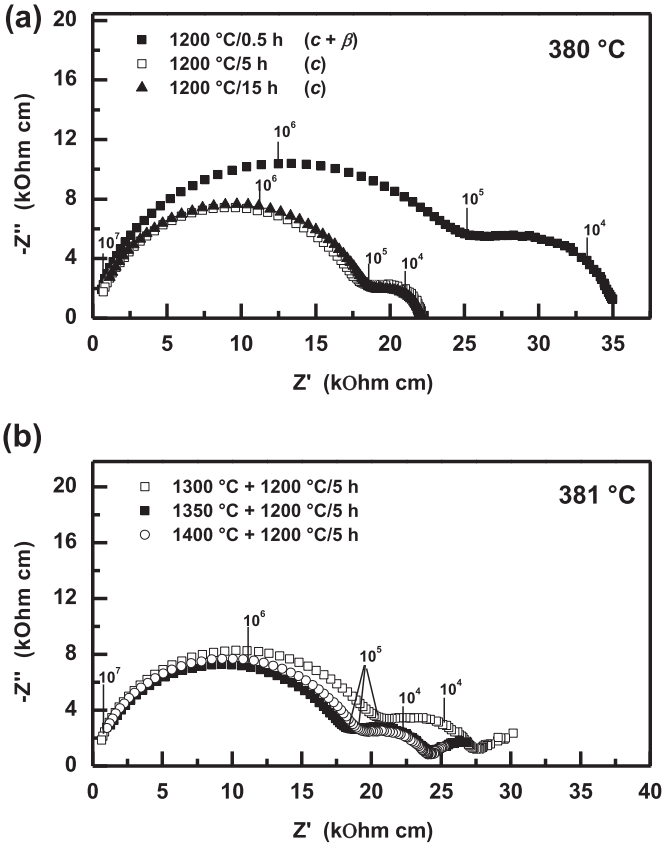


**Fig. 12.** Impedance spectroscopy diagrams of 10Sc1CeSZ sintered by (a) conventional and (b) two-stage methods.

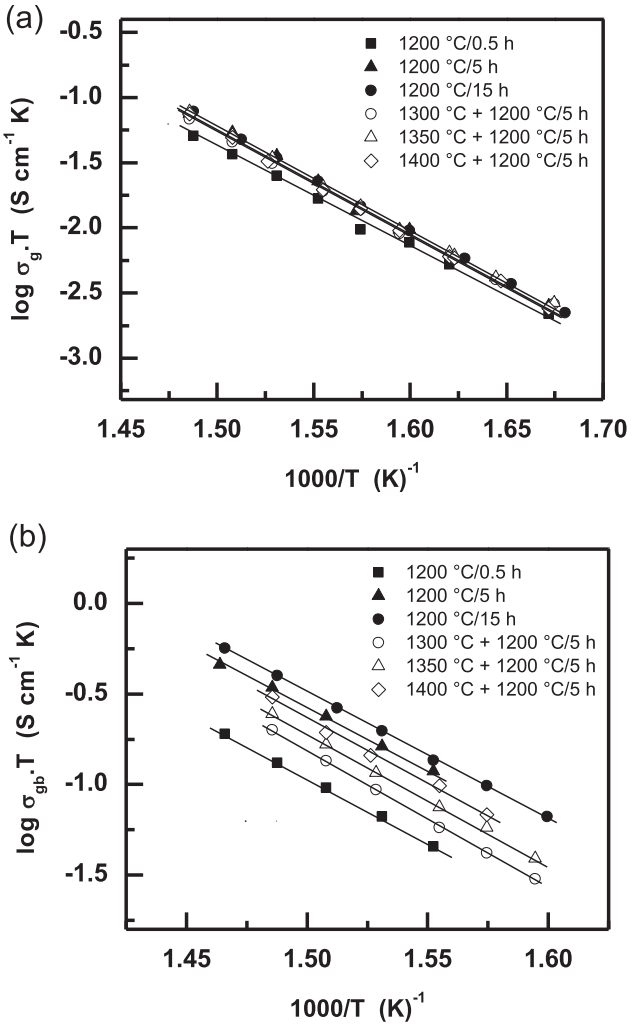


**Fig. 13.** Arrhenius plots of (a) grain and (b) grain boundary conductivities.

a gradual increase of the grain boundary conductivity. Thus, the observed differences in the grain boundary conductivity of 10Sc1CeSZ pellets may be primarily related to the grain boundary density (grain boundary per unit area).

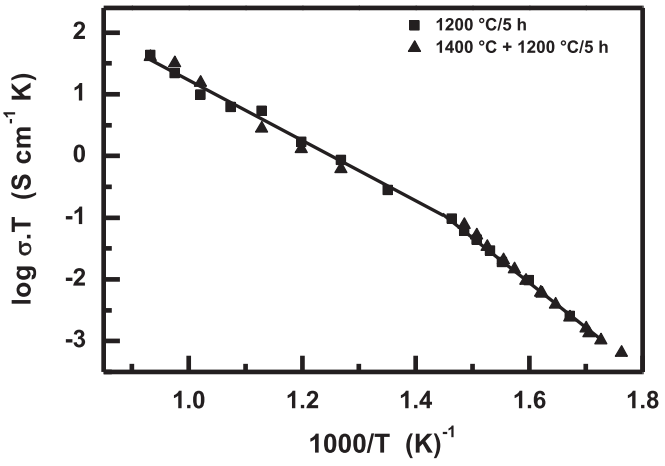


**Fig. 14.** Temperature dependence of the overall electrolyte conductivity. The lines are only guide for eyes.

Fig. 14 shows the temperature dependence of the overall electrolyte conductivity of 10Sc1CeSZ samples sintered at 1200 °C for 5 h (conventional method) and 1400 °C followed by 1200 °C for 5 h (two-stage method).

The change of slope occurs at ~500 °C. This change was attributed to a combined effect of association between dopants and oxygen-ion vacancies and ordering due to microdomain formation at low temperatures [18]. The activation energy values for conduction obtained by fitting of the experimental results are 1.5 ± 0.1 (low temperature) and 1.0 ± 0.1 eV (high temperature) independent on the sintering method. The overall ionic conductivity in the high-temperature range (~$1.5 \times 10^{-2}$ S cm$^{-1}$ at 700 °C) determined by impedance spectroscopy is similar to that in previous works [9,15]. In the low-temperature range the obtained values (~$2.7 \times 10^{-4}$ S cm$^{-1}$ at 450 °C) are of the same order of magnitude of those in Refs. [19,20], and minor differences are assigned to specific sintering conditions.

## 4. Conclusions

10Sc1CeSZ solid electrolyte is found to be structurally stable up to 1000 °C. Under isothermal conditions, the total linear shrinkage amounts 21% up to 1380 °C with maximum rate at 1180 °C. In conventionally sintered specimens with null holding time, full density (>99%) is attained for temperatures above 1350 °C with simultaneous stabilization of the cubic structure. In the 1150–1300 °C range a combination of cubic and rhombohedric phases prevails. Increase of the holding time promotes the rhombohedric-to-cubic phase transition. For high sintering temperatures and longer holding times, degradation of the cubic structure occurs.

The two-stage sintering method can be used to obtain dense 10Sc1CeSZ solid electrolyte with reduced grain sizes compared to the traditional method of sintering. In this case, $T_1$ determines the crystalline structure.

The grain conductivity of pellets sintered by these methods does not show any significant difference. The blocking effect at the grain boundaries is primarily dependent on the mean grain size.

## Acknowledgments

To FAPESP, CNEN and CNPq for financial supports and to CCCH at IPEN for thermodilatometry experiments. One of the authors (R.L.G.) acknowledges CAPES for the scholarship.

## References

[1] Y. Mizutani, M. Tamura, M. Kawai, O. Yamamoto, Solid State Ionics 72 (1994) 271–275.
[2] O. Yamamoto, Y. Arati, Y. Takeda, N. Imanishi, Y. Mizutani, M. Kawai, Y. Nakamura, Solid State Ionics 79 (1995) 137–142.
[3] Y. Arachi, H. Sakai, O. Yamamoto, Y. Takeda, N. Imanishi, Solid State Ionics 121 (1999) 133–139.
[4] S.P.S. Badwal, F.T. Ciacchi, D. Milosevic, Solid State Ionics 136/137 (2000) 91–99.
[5] R. Ruh, H.J. Garret, R.F. Domagala, V.A. Patel, J. Am. Ceram. Soc. 60 (1977) 309–403.
[6] K. Nomura, Y. Mizutani, M. Kawai, Y. Nakamura, O. Yamamoto, Solid State Ionics 132 (2000) 235–239.
[7] S.P.S. Badwal, F.T. Ciacchi, S. Rajendran, J. Drennan, Solid State Ionics 109 (1998) 167–186.
[8] Y. Arachi, T. Asai, O. Yamamoto, Y. Takeda, N. Imanishi, K. Kawate, C. Tamakoshi, J. Electrochem. Soc. 148 (2001) A520–A523.
[9] Z. Wang, M. Cheng, Z. Bi, Y. Dong, H. Zhang, J. Zhang, Z. Feng, C. Li, Mater. Lett. 59 (2005) 2579–2582.
[10] D.-S. Lee, W.S. Kim, S.H. Choi, J. Kim, H.-W. Lee, J.-H. Lee, Solid State Ionics 176 (2005) 33–39.
[11] H. Tu, X. Lin, Q. Yu, J. Power Sources 196 (2011) 3109–3133.
[12] S. Yarmorlenko, J. Sankar, N. Bernier, M. Klimov, J. Bapat, N. Orlovskaya, J. Fuel Cell Sci. Technol. 6 (2009) 021007.
[13] N. Orlovskaya, S. Lukish, G. Subhash, T. Graule, J. Kuebler, J. Power Sources 195 (2010) 2774–2781.
[14] M. Kleitz, J.N. Kennedy, Resolution of multicomponent impedance diagrams, in: P. Vashishta (Ed.), Fast Ion Transport in Solids, Electrodes and Electrolytes, North Holland, New York, 1979, pp. 185–188.
[15] A. Heel, A. Vital, P. Hostappels, T. Graule, J. Electroceram. 22 (2009) 40–46.
[16] M.A. Laguna-Bercero, S.J. Skinner, J.A. Kilner, J. Power Sources 192 (2009) 126–131.
[17] I.W. Chen, X.W. Wang, Nature 404 (2000) 168–171.
[18] T.I. Politova, J.T.S. Irvine, Solid State Ionics 168 (2004) 153–165.
[19] M. Liu, C. He, J. Wang, W.G. Wang, Z. Wang, J. Alloys Compd. 502 (2010) 319–323.
[20] S. Omar, W.B. Najib, N. Bonanos, Solid State Ionics 189 (2011) 100–106.